AIAA SciTech Forum
8-12 January 2024, Orlando, FL
AIAA SCITECH 2024 Forum

10.2514/6.2024-1842

Dynamic Deployment of Foldable Composite Structures with Pre-Tensioned Springs

Alexandra Haraszti*, Narravula Harshavardhan Reddy†, and Sergio Pellegrino‡
California Institute of Technology, Pasadena, CA

Deployable solar arrays for the Caltech Space Solar Power Project consist of ladder-like strips of thin-shell composites and use a dynamic, unconstrained deployment scheme. We study the effect of pre-tensioned springs within these structures on the successful completion of their deployment (latching), focusing on a single folded rectangular frame. We tune a finite element model in order to predict deployment timing and latching, and develop an analytical model to identify intermediate equilibrium states for the structure that may prevent full deployment. Our findings suggest that for equivalent pre-loads, the constant-force springs utilized in the current strip architecture generate significantly larger resisting moments and act earlier in the deployment compared to linear spring alternatives, thereby increasing the likelihood of unsuccessful deployment.

I. Nomenclature

ϕ	=	longeron flange angle
θ	=	fold angle. $\theta = 0$ when strip is unfolded
θ_0	=	initial fold angle
θ_c	=	critical fold angle: deployment fails for $\theta_0 < \theta_c$
a	=	spring offset from longeron web surface
D	=	distance between fixed hanging points
d_{CM}	=	horizontal distance between strip hinge and half-strip center of mass
e	=	spring extension
e_0	=	spring extension when the strip is fully unfolded
F	=	axial force in spring
F_0	=	axial force in spring when the strip is fully unfolded
f	=	projected spring force in plane of longeron
H	=	length of hanging cords
I	=	rotational inertia of one half of the strip
L	=	base length of strip
M_{spring}	=	applied moment at fold due to springs
M_{strip}	=	internal strip moment at fold
M_{tot}	=	total moment in strip at fold
R	=	radius of longeron flanges
r	=	distance from a point on the strip to the axis of rotation
s	=	curvi-linear strip coordinate. $s = 0$ at center of strip
t	=	time since deployment initiation
W	=	height of longeron web

*Currently Ph.D. Student, Aeronautics and Astronautics, Stanford University, Stanford, CA 94305. AIAA Student Member. haraszti@stanford.edu.
†Currently Mechatronics Engineer II, Jet Propulsion Laboratory, California Institute of Technology, Pasadena, CA 91109. AIAA Young Professional Member
‡Joyce and Kent Kresa Professor of Aerospace and Civil Engineering, Jet Propulsion Laboratory Senior Research Scientist; Co-Director, Space-Based Solar Power Project, Graduate Aerospace Laboratories, 1200 E. California Blvd., Mail Code 105-50. AIAA Fellow. sergiop@caltech.edu

II. Introduction

In contrast with controlled deployment methods, where deployment is continuously actuated and quasi-static, unconstrained deployment schemes for deployable structures are highly dynamic and more difficult to predict. However, unconstrained deployment methods can greatly simplify the design of the deployment mechanism, reducing mass, complexity, and cost.

The Caltech Space Solar Power Project is a concept for harnessing solar energy in space and transmitting it back to Earth by use of deployable space-based solar arrays that are tens of meters in size. These solar arrays utilize an unconstrained deployment scheme and are the topic of this work. The array deployment consists of a quasi-static uncoiling of the structure from a central hub, followed by a dynamic, uncontrolled unfolding step powered by the release of elastic strain energy stored in the structure (Fig. 1) [1].

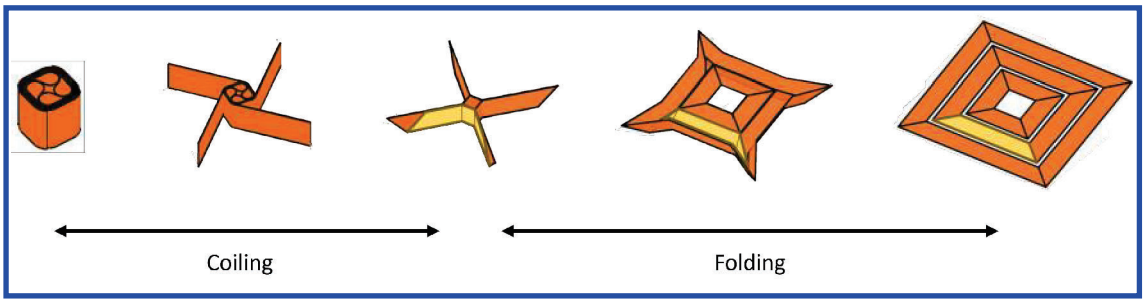

Fig. 1 The unfolding portion of the SSPP array deployment happens in one unconstrained dynamic step [2].

The solar array architecture consists of composite ladder-like strips supporting pre-tensioned membranes carrying PV and RF functional elements [3]. These strips are of trapezoidal shape and are arranged into four symmetric quadrants to form a square array. One such quadrant with a highlighted strip is shown in Fig. 2.

For each ladder-like strip, the ladder rails consist of two composite triangular rollable and collapsible (TRAC) longerons [4] (Fig. 2). TRAC longerons have a flat web connecting two circular arc flanges in a geometry that provides high stiffness to weight ratio while being foldable and rollable if the flanges are flattened. The webs of the two longerons are connected by composite rectangular battens which provide structural stiffness and create the ladder rungs. Each set of two consecutive battens forms an enclosed rectangular bay, called a frame, which supports the membrane.

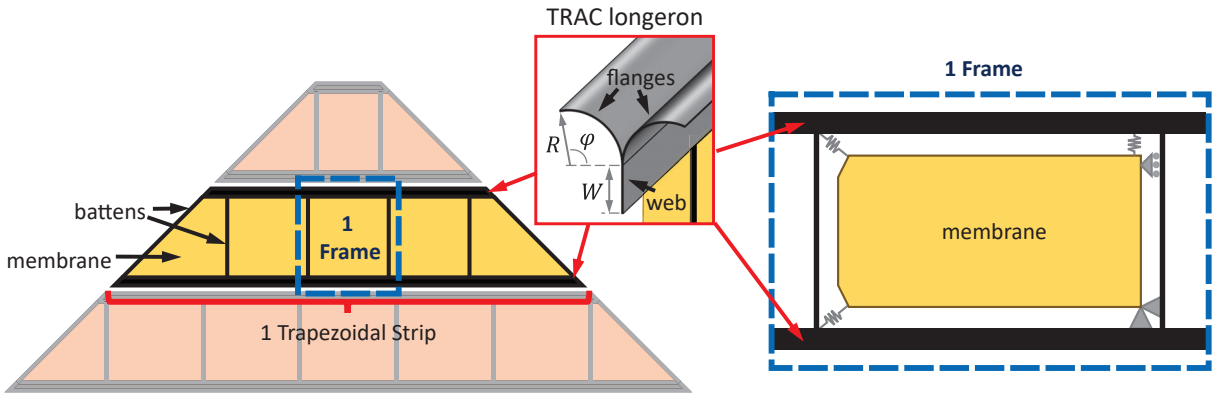

Fig. 2 The strip architecture for SSPP consists of two TRAC longerons connected by composite battens.

In low earth orbit, the structure would be subjected to a temperature range of -70^oC to 50^oC, causing thermal deformations in the longerons and membrane [5]. Due to the difference in thermal properties of the membrane and composite longerons, such thermal loads may place the membrane under compression, causing wrinkling and adversely affecting its function. An approach for limiting compression in the membrane is to apply pre-tension to the membrane within each frame when it is attached to the outer structure at room temperature.

In the current architecture discussed in [5], the membrane is pre-tensioned using extension springs at three corners according the the schematic in Fig. 2. The pre-tension is achieved using kirigami springs which gain their mechanical

properties from a geometric cut pattern that buckles out-of-plane upon extension [6]. These springs were chosen for their flexibility and flat profile that does not interfere with the folding and coiling of the structure. Kirigami springs have two mechanical regimes, during the second of which they are approximately constant-force (Fig. 3b).

The stowing mechanism for the structure creates a nearly 90^o fold at the center of the strip longerons, flattening the longeron flanges and storing elastic strain energy (Fig. 1). During the deployment process, all strips unfold simultaneously. This process is powered only by the release of strain energy stored in the fold. The effect of the pre-tensioned springs on the final stages of the deployment has not yet been studied.

Since the deployment of the full array is complex due to the size and number of parts involved, previous work to study the behavior of elastic folds in the ladder-like strips utilized a simpler symmetric rectangular strip [1]. In this study, we extend this prior work to examine the effect of spring pre-tension on the self-powered deployment of a foldable ladder-like composite strip. To circumvent the complexity of a tensioned membrane, extension springs and cords were used in place of a Kapton membrane.

By fine-tuning the spring geometry, initial extension, and the starting fold angle for deployment, we sought to determine the critical threshold at which the strip could no longer overcome the spring forces and achieve complete deployment. To validate our findings, we conducted both experimental tests on fabricated strips and utilized finite element deployment models, extending the work in [1]. Our results suggest that while dynamic deployments starting from large fold angles are usually successful, ensuring deployment even under quasi-static conditions requires the spring forces and extensions to be small such as to prevent intermediate static equilibrium states during unfolding. Constant force and near-constant force springs generate larger moments applied moments than linear springs and are thus most likely to prevent the structure from reaching complete deployment.

III. Analytical Model

To examine the impacts of pre-tension on strip deployment, we consider a simple model for one square frame of a rectangular ladder-like strip consisting of two longerons with spacing L, two composite battens with spacing L, and two extension springs (one on each frame diagonal). The strip is folded such that the longerons hinge about the center of the frame (Fig. 3a).

We use identical kirigami springs for the extension springs. Kirigami springs have two mechanical regimes resulting in a roughly piecewise linear force-to-extension relationship. The first regime for small spring extensions has a high spring constant, followed by a "plateau" second regime where the spring is nearly constant force (Fig. 3b).

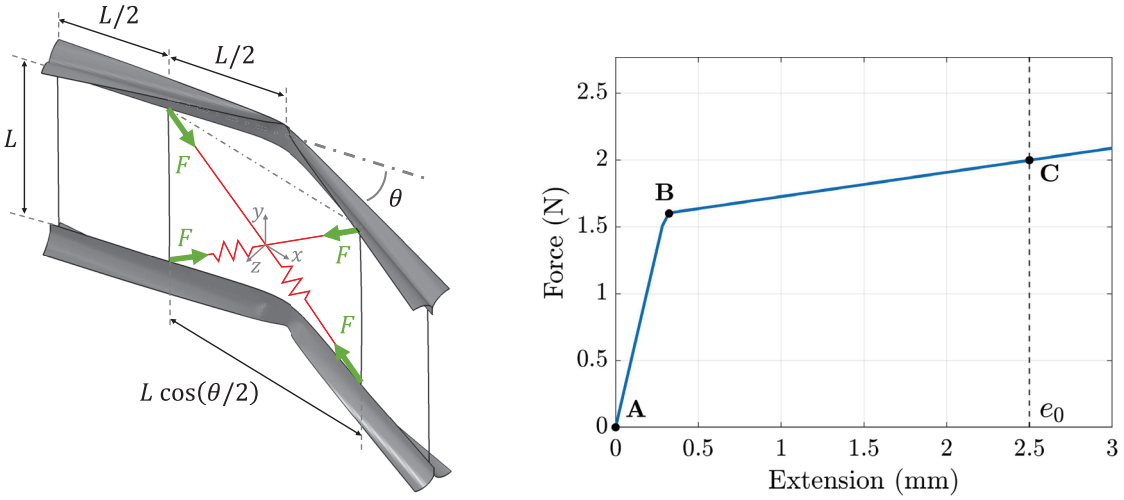

(a) One frame of a folded strip unfolding under pre-tension

(b) The kirigami spring force-extension curve can be approximated as bi-linear

Fig. 3 Folded configuration of frame and force-extension relationship of kirigami spring

For simplicity, we assume the springs lie in the plane of the strip, and the force generated by the springs remains in the plane formed by the four corners of the frame, even as the strip is folded by angle θ.

We can relate the force-extension relationship of the spring to the moment exerted on the strip by the springs for a given fold angle by analyzing the strip's geometry. Given an initial spring extension e_0, the extension in terms of fold angle θ can be calculated as

$$e(\theta) = L\sqrt{1 + cos^2(\theta/2)} - L\sqrt{2} + e_0. \tag{1}$$

Spring force F is a function of the spring extension e, and this relationship must be measured experimentally. Then let f be the sum of spring forces F projected onto the horizontal x-z plane

$$f(\theta) = 2F\frac{cos(\theta/2)}{\sqrt{1 + cos^2(\theta/2)}}. \tag{2}$$

Then the moment M_{spring} about the hinge is given by

$$M_{spring}(\theta) = \frac{fL}{2}sin(\theta/2). \tag{3}$$

Thus, given the known force-extension relationship of the spring, we have obtained an expression for the moment at the hinge due to the springs.

For a simplified bi-linear force-extension curve representative of a kirigami spring, the corresponding moment-angle relationship is shown in Fig. 4. For example, consider an initial extension of $e_0 = 2.5$ mm when the strip with base length $L = 200$ mm is fully unfolded. For a strip folded past $\theta = 21.6^o$, the springs start out slack. As the frame unfolds, the springs hit their rest length and begin to extend (Point **A**). This is accompanied by a sharp increase in moment, as the springs deform in their first regime. At Point **B**, the springs transition into their second mechanical regime. At the same time, as θ approaches zero, the moment arm decreases until the strip is fully unfolded, the springs reach their full extension, and the moment becomes zero (Point **C**).

We compare this moment-angle relationship to that due to the internal strain in the pinched longerons of the strip. We can obtain this internal moment by performing a rotation-controlled quasi-static unfolding simulation of the strip in the Abaqus finite element software. For large fold angles, the longeron flanges are flattened and the strip folds like a hinge: the internal moment is small and roughly constant. At approximately $\theta = 12^o$, the longerons latch, meaning the flanges unfold. This causes a sharp increase in moment, followed by a roughly linear decrease to zero as the strip reaches full deployment. We define a successful deployment as one where both longerons latch.

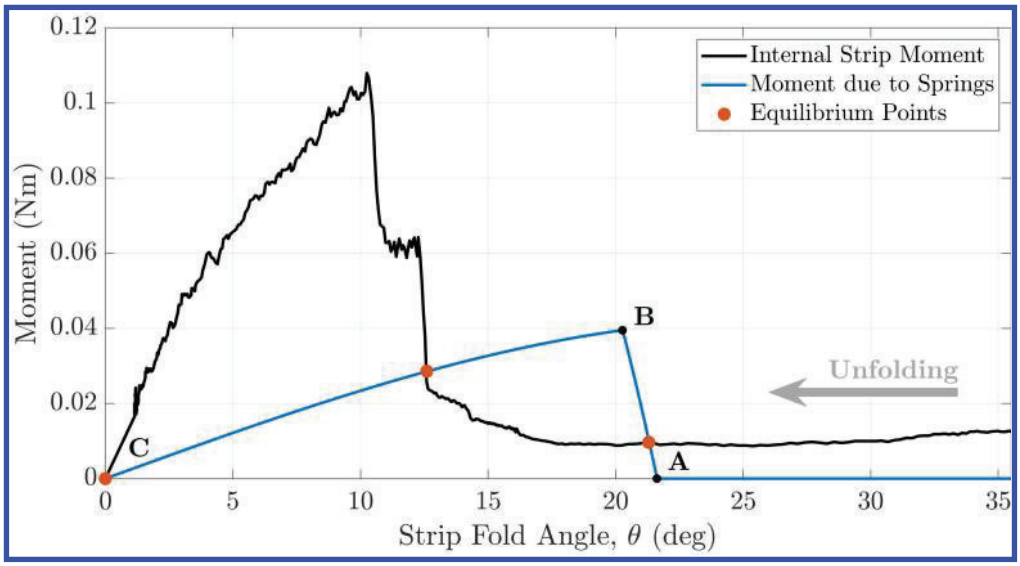

Fig. 4 Opposing moments due to springs and internal strain energy during quasi-static unfolding of strip under pre-tension. Moment magnitudes are plotted for clarity. For this architecture, the strip has two intermediate equilibrium points where the total moment is zero.

Comparing the two competing moments, we observe that for this strip and spring geometry, the spring moment is largest when the internal moment is still small. Further, we identify two equilibrium points where the total moment in

the strip will be zero. The first of these, at the larger fold angle, is a stable equilibrium point, and the second at a smaller fold angle is unstable. In order for the strip to successfully deploy quasi-statically, we would require that the moment due to the spring force must never exceed the strip's internal moment. If this is not the case, in order for the strip to unfold dynamically, the strip must start out with a large enough fold angle so that the springs start slack, and must gain enough rotational kinetic energy to overcome the effect of the springs. The unfolding will be examined experimentally, numerically and analytically in the following sections.

IV. Methods

A. Experimental

The TRAC longerons for the test strip were fabricated according to the composite layup and techniques developed in [7]. The flanges have ply order $[\pm 45_{GFPW}/0_{CF}/\pm 45_{GFPW}]$ and the web has ply order $[\pm 45_{GFPW}/0_{CF}/\pm 45_{3,GFPW}/0_{CF}/\pm 45_{GFPW}]$, where CF is unidirectional Pyrofil MR 70 12P carbon fibers made by Mitsubishi Chemical, and GFPW is plain weave scrim glass. The plies were impregnated with ThinPreg 415 resin made by North Thin Ply Technology [8]. The longerons were fabricated to have nominal flange radius $R = 13.7$ mm, flange angle $\phi = 105^o$, and web height $W = 8$ mm. Two longerons cut to 400 mm were connected by pultruded carbon fiber battens bonded with epoxy to the webs to achieve a ladder-like strip with longeron spacing of $L = 200$ mm.

In order to decrease the effects of gravity on the structure's deployment, we suspended it on its side such that it unfolds in a plane neutral to gravity. We hung the structure from cords of length $H = 1000$ mm fixed to the two inner battens. The cords were routed around the longerons using foam dowels to avoid interference. In order to minimize tipping and swinging, we determined the strip dimensions such that the hanging points fall roughly in line with the strip's center of mass even when folded (Fig. 5a). The upper ends of the hanging cords were tied to a rail at a distance $D = 175$ mm from each other. Since the upper ends of the cords are fixed and the lower ends move closer together as the strip is folded, if $D > L$, the cords may aid unfolding. Conversely, if $D << L$, the cords may hinder unfolding. Therefore, D was chosen to be slightly less than L with $D, L < H$ to minimally impact unfolding for a variety of initial fold angles. The strip and setup dimensions are given in Table 1.

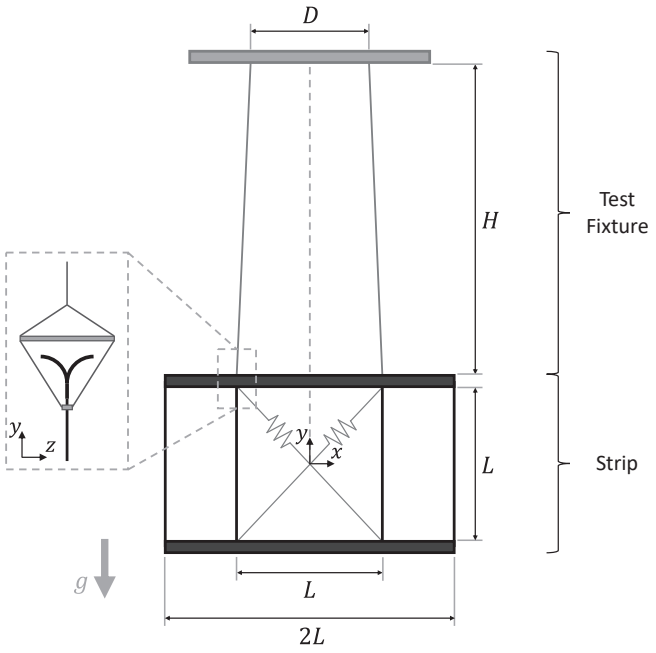

(a) Experimental setup

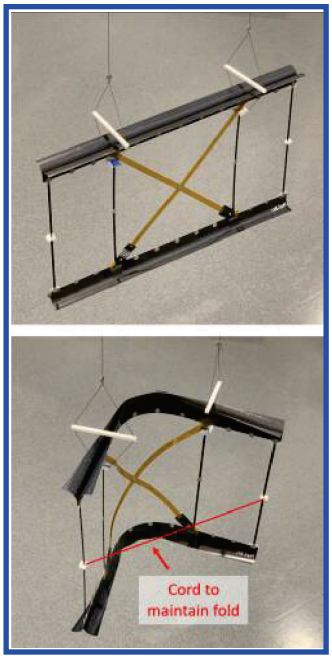

(b) Unfolded (top) and folded (bottom) strip

Fig. 5 The experiment is designed to minimize the effects of gravity on unfolding.

Table 1 Strip Dimensions

Setup		Longeron	
L	200 mm	R	13.6 mm
H	1000 mm	ϕ	105^o
D	175 mm	W	8 mm

The hanging strip was folded by pinching the longerons in the center and then tying a cord in between the center of the outermost battens to enforce the fold (Fig. 5b). Deployment was initiated by cutting this cord with scissors.

The deployment of the test strip was recorded with six NaturalPoint OptiTrack Prime 41 motion capture cameras [9] distributed around the strip. The unfolding was recorded at 250 frames per second. Each longeron web was outfitted with 13 equally distributed retroreflective markers, along with additional markers on the battens and cords. The positions of these markers in each frame was reconstructed using the commercial Motive software [9].

The longeron fold angle was calculated for both the upper and lower longeron for every time step. Since the longeron deformation due to folding is localized to the inner frame, this was achieved by fitting a line to the outermost three web marker coordinates of either side of a longeron, and then calculating the angle between the two sides.

1. Kirigami Springs

Kirigami springs were laser cut out of 100 μm thick 1095 Stainless steel based on the cut pattern shown in Fig. 6a. Four springs each of two different geometries (given in Table 2) were characterized using an Instron tension test (Fig. 6b). At an extension of 2.5 mm, Spring 1 had a load of 1.4 N and Spring 2 had a load of 2 N. Both spring patterns showed repeatability between repeated laser cuts of the same geometry and multiple cycles.

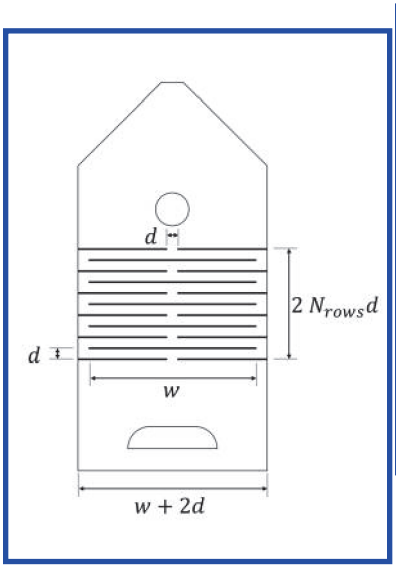

(a) Cut pattern for kirigami spring

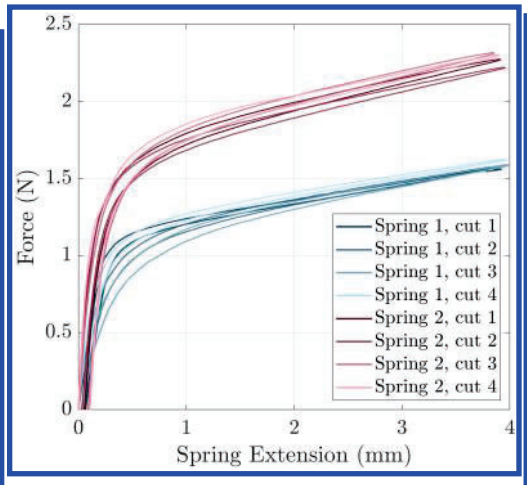

(b) Four identical springs were laser cut and underwent tension testing for two different spring geometries. The tests show consistency between consecutive cuts of the same geometry.

(c) Spring fastened to longeron and pre-tensioned

Fig. 6 The force-extension behavior of each laser cut spring was characterized using a tension test. Two springs of the same type were fastened to the strip diagonals for testing.

To allow for removable and interchangeable springs, the springs were attached to the longerons using low profile Dual-Lock mushroom head fasteners made by 3M. These fasteners offset the springs from the longeron web surface by a = 1.25 mm. Thin strips of 50 μm thick Kapton was used to span the frame diagonals. The strip was clamped to a stretching fixture to extend the springs by 2.5 mm before fastening. An extended spring is shown in Fig. 6c.

All further results in this paper are for experiments with Spring 2. The average force-extension relationship from the four tested springs was used in the numerical model.

Table 2 Kirigami Spring Dimensions

Dimension	Spring 1	Spring 2
N_{rows}	5	5
w [mm]	15	14.5
d [mm]	1	1.2

B. Analytical Deployment Model

Following the moment analysis in Section III, we update Equations 1-3 to reflect the spring offset from the longeron web surface by $a = 1.25$ mm (see Fig. 7). For this section, we re-define θ relative to half the strip, such that the total fold angle is 2θ. The spring extension becomes

$$e(2\theta) = \sqrt{L^2 + (L\,cos(\theta) - 2a\,sin(\theta))^2} - L\sqrt{2} + e_0. \tag{4}$$

The total spring force in the x-z plane is given by

$$f(2\theta) = 2F\frac{L\,cos(\theta) - 2a\,sin(\theta)}{\sqrt{L^2 + (L\,cos(\theta) - 2a\,sin(\theta))^2}}. \tag{5}$$

Then the moment M_{spring} about the hinge is

$$M_{spring}(2\theta) = f(2\theta)\left(\frac{L}{2}sin(\theta) + a\right). \tag{6}$$

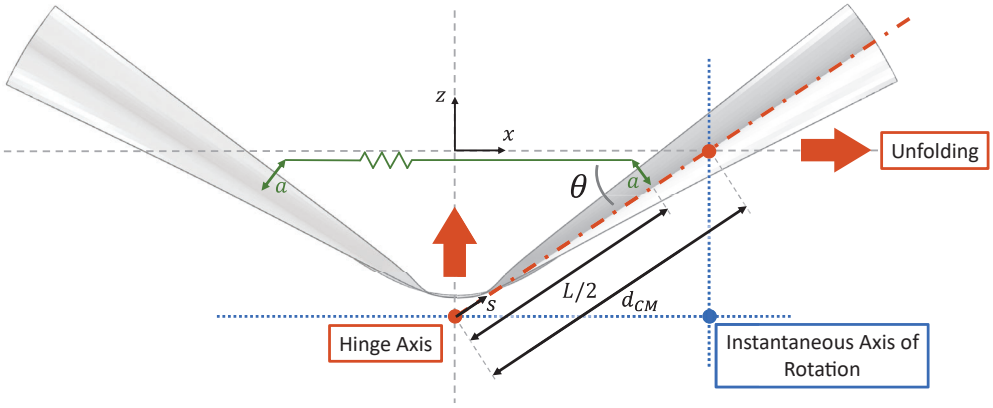

Fig. 7 2D top view of unfolding strip. We calculate the instantaneous center of rotation for the right side for any θ in order to derive the strip moment of inertia as a function of θ. The springs are offset from the longeron web surface by a.

Given the internal strip moment M_{strip} obtained from FEM, we can write the total moment in the strip at the fold as

$$M_{tot} = M_{spring} - M_{strip}. \tag{7}$$

To obtain the strip's fold angle as a function of time, we apply Newton's second law $\tau = I\alpha$, where τ is torque, I is rotational inertia, and α is angular acceleration. In our case, this yields the initial value problem

$$M_{tot}(2\theta(t)) = I(\theta(t))\frac{d^2\theta(t)}{dt^2} \tag{8}$$

where the initial conditions are zero angular velocity, and a given initial fold angle.

In order to solve the problem, we first need an estimate of the rotational inertia of the strip. Examining just one side of the strip to the right of the hinge, we can approximate the center of the mass, d_{CM} of the half-strip as being a distance

$$d_{CM} = \frac{L\, m_{longeron} + L/2\, m_{batten} + L\, m_{batten}}{2m_{longeron} + 2m_{batten}} \tag{9}$$

along the longeron away from the hinge. The motion of the unfolding strip will be constrained as follows: the hinge travels only in the negative z-direction, and the center of mass will travel only in the positive x-direction (Fig. 7). The instantaneous center of rotation of the half-strip is then given by

$$x_{axis}(\theta) = d_{CM}\, cos\theta, \quad z_{axis}(\theta) = -d_{CM}\, sin\theta \tag{10}$$

We can also parametrically define the location of any point on the strip by its curvi-linear coordinate s starting from the center as

$$x(\theta, s) = s\, cos\theta, \quad z(\theta, s) = (s - d_{CM})\, sin\theta \tag{11}$$

The distance of any point on the strip from the axis of rotation at any given fold angle is thus given by

$$r(\theta, s) = \sqrt{[(s - d_{CM})\, cos\theta]^2 + [s\, sin\theta]^2} \tag{12}$$

Using this formula, and the mass of the individual strip elements, the calculations for the rotational inertias of the individual components of the strip are shown in Table 3. The mass of each element was measured before assembling the experimental setup.

Table 3 Mass and Inertial Properties for Half-Strip

Part	**Mass, m (g)**	**Rotational Inertia (total for half-strip)**
Longerons (×2)	1.5703	$\frac{m}{L}\int_0^L r(\theta, s)^2 ds$
Inner Batten	0.5796	$mr(\theta, L/2)^2$
Outer Batten	0.5796	$mr(\theta, L)^2$
Epoxy (×2)	0.135	$mr(\theta, L/2)^2 + mr(\theta, L)^2$
Spring	0.414	$mr(\theta, L/2)^2$
Velcro (×2)	0.153	$mr(\theta, L/2)^2$
Kapton (×2)	0.1625	$\frac{m}{L}\int_0^{L/2} r(\theta, s)^2 ds$

Finally, we use Mathematica's numerical initial value problem solver `NDSolve` to obtain an analytical solution for $\theta(t)$.

C. Numerical Deployment Model

Finite element simulations of the deployment were performed using the Abaqus/Explicit dynamic solver. The longerons were modeled using S4R shell elements with a mesh size of 2 mm (11,200 total elements). To capture the behavior of the composite longerons, an experimentally determined **ABD** stiffness matrix was used for the web and flanges respectively [8]. B31 beam elements were used for the battens and the battens were joined to the longerons using coupling constraints. The Kapton strips were represented with homogeneous S4R shell elements with mesh size 4 mm. Axial connectors were used for both the hanging cords (rigid) and extension springs (non-linear extension-coupled force). The spring connector rest length was set 2.5 mm shorter than the actual length to simulate the pre-tension.

The simulation was carried out under gravity and can be broken down into five steps, as shown in Fig. 8. Similar to the simulation procedures used in [1, 8], the first four of these steps simulate the folding process, during which localized folds were first created at the center of the two longerons by applying a pressure that flattens the flanges. Rotational displacements were applied to fold the strip. Once the fully folded configuration has been reached, residual kinetic energy was dissipated in order to begin the deployment from a static condition. This was achieved through viscous damping applied to all longeron surfaces. In step (5), the displacement constraint on the outer battens was

instantaneously removed allowing the strip to self-deploy. The only boundary condition in this step was the fixed ends of the hanging cords.

It has been previously shown [1] that air drag on the longeron surfaces has a minimal effect on deployment so it was neglected in this model.

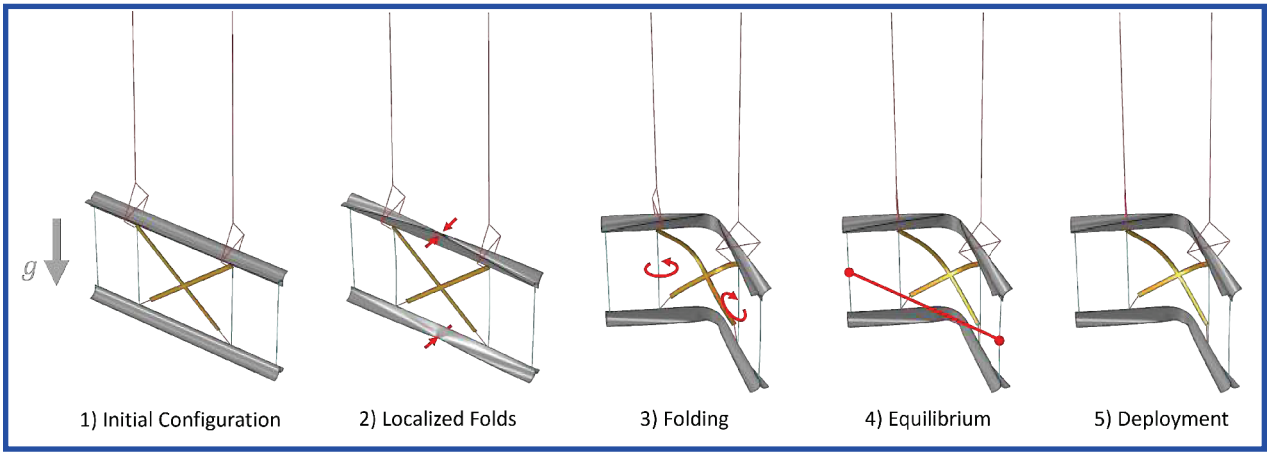

Fig. 8 Simulation procedure: Localized folds are created by pinching the longeron flanges (2), then the strip is folded to the desired angle by applying rotational displacements to the longerons (3) and held stationary until kinetic energy from folding is dissipated (4). The folding constraints are removed and the strip deploys (5).

V. Results and Discussion

To quantify the unfolding behavior of the strip, we tracked the fold angle of the upper and lower strip longerons over time for both the FEM and experiments, using the experiments to validate the FEM results. We also compare these results to the integrated analytical model. A fully deployed strip has fold angle $\theta = 0$. Due to the frame rate of the motion capture cameras, the exact time when deployment begins can only be aligned with the models within 0.004 seconds. In order to improve comparisons, the timing of the motion capture results was shifted by $-0.004 < dt < 0.004$ seconds such that the mean square error in angle in between the FEM and experiment up until latching was minimized.

Across multiple experiments from different initial angles, θ_0, we aim to approximate the critical angle, θ_c, such that for $\theta_0 < \theta_c$, the longerons do not latch and the strip fails to fully unfold.

A. Strip without springs

Before tackling the deployment of a strip with tensioned springs, we first validated the FEM and analytical model on the unfolding of a strip without springs. Across various initial fold angles, deployment took on the order of 0.05 seconds and the FEM captured the motion within 4^o for each trial (Fig. 9). The analytical model was slightly worse, with a maximum error of 8^o for the largest θ_0. In all trials, after the longeron flanges latched, the strip angle oscillations decreased to under $\pm 1^o$ in under 0.08 seconds.

As expected, larger initial angles took longer to reach full deployment and thus matching the model's start angle to the experiment was paramount for valid results. Because the strip is very lightweight (8.6 g for longerons and battens), all additional masses such as the retroreflective markers, bonded epoxy joints, and foam cord connectors (1.3 g total) were accounted for as point masses in the model.

Since the first steps in the simulation correspond to the folding of the strip, we also validated the folded shape achieved with simulations by comparing the relative positions of the 13 upper and lower longeron markers with experiments for the same initial fold angle. Since the motion capture and FEM are conducted in different coordinate systems, the first step was registering the marker point clouds at $t = 0$ using a rigid body transformation. Then the motion capture coordinates were transformed onto the FEM coordinates for all time steps. As the longerons unfold, we compared the displacements of each marker from the fully folded state to the latched state and observe an extremely close match between the FEM and experiments. For example, the initial configuration, final configuration, and unfolding trajectory from $\theta_0 = 134^o$ for the strip is shown in Fig. 10.

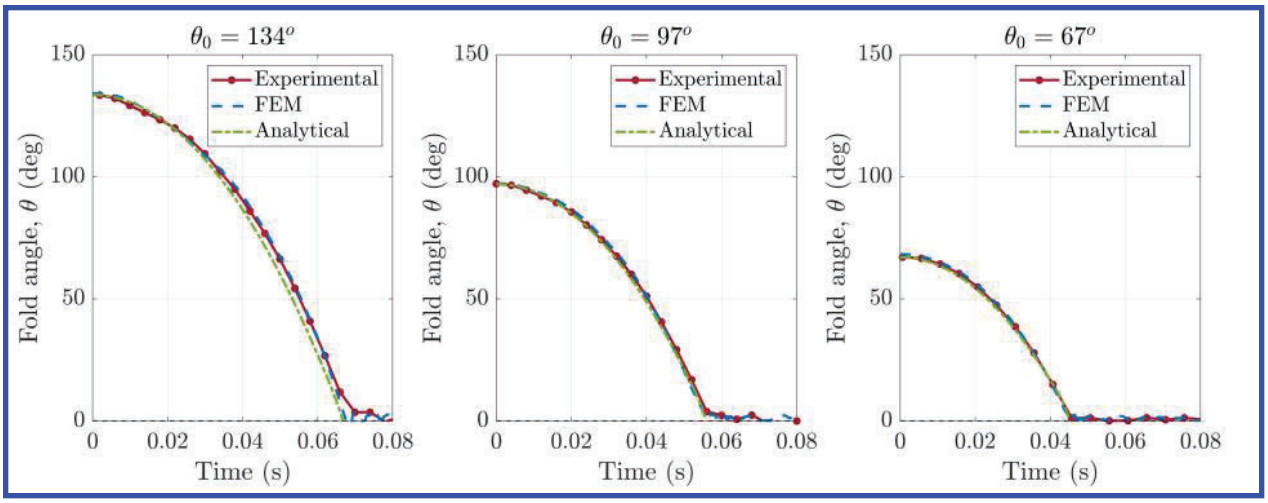

Fig. 9 For a strip unfolding without springs, we observe strong alignment between the two models and the experimental results with a maximum error of 3.85^o. The average fold angle of the two longerons is plotted for clarity.

B. Strip with springs

The strip was pre-tensioned with diagonal springs, each extended to 2.5 mm to achieve a pre-load of 2N. Unfolding experiments were performed at decreasing initial fold angles until the deployment was unsuccessful. Four initial fold angles were tested (72^o, 57^o, 48^o, and 45^o), the angles being defined by 1 cm decreases in the length of the cord tied across the battens to fold the strip. Deployment was unsuccessful for fold angles of $\theta_0 = 48^o$ and 45^o: the longerons failed to latch, and the strip eventually came to rest with a fold angle of 19^o in the upper longeron and 25^o in the lower longeron. Data from three initial fold angles is shown in Fig. 12. Even when the deployment was successful for larger fold angles, the effect of the springs was visible as a deceleration in the unfolding before latching. The lower longeron lagged behind the upper one, potentially due to a spring mass being concentrated there. The FEM and analytical models were calculated for these initial fold angles.

1. Analytical Model vs. Experiments

The results from the analytical model predict latching for all experimentally tested angles, and the model predicts slower unfolding than the experiments in all three trials. Very little deceleration due to springs is seen, even for the smallest initial fold angle (Fig. 11). Since the analytical model does not differentiate between longerons, it cannot capture the asymmetries in unfolding between the upper and lower longerons.

As a validation for the integration in the analytical model, a simplified FEM was created without the Kapton strips. Instead, the spring connectors extended all the way across the frame, as shown for the analytical model in Fig. 3a. The Kapton and spring mass was distributed to point masses at the ends of the connectors. The results of this FEM are also plotted in Fig. 11 and match with the predicted latching times of the analytical model within 3 milliseconds. The shape of the curve is different however, with the simplified FEM matching within 1^o of the experimental results up until $t = 0.03$ s whereas the analytical model lags behind by a maximum of 7^o.

Neither the analytical model nor the simplified FEM account for the partial coupling of the spring extensions due to the intersection of the Kapton strips, nor the inertial out-of-plane swinging of the Kapton as the strip unfolds, which was observed in slow motion videos of the strip unfolding. The errors between these simplified models and experimental results suggest that capturing these dynamics is crucial for an accurate model. Thus, we opted to use the analytical model only for static analysis and further refine the FEM to better match the experimental results.

2. FEM vs. Experiments

For the first approximately 0.03 seconds of the deployment, when the springs are slack, the FEM followed the experimental data within 1^o (Fig. 12). However, the structure fully deployed for all θ_0 in the FEM, although the deceleration due to the springs became more and more pronounced, extending the latching time difference between the

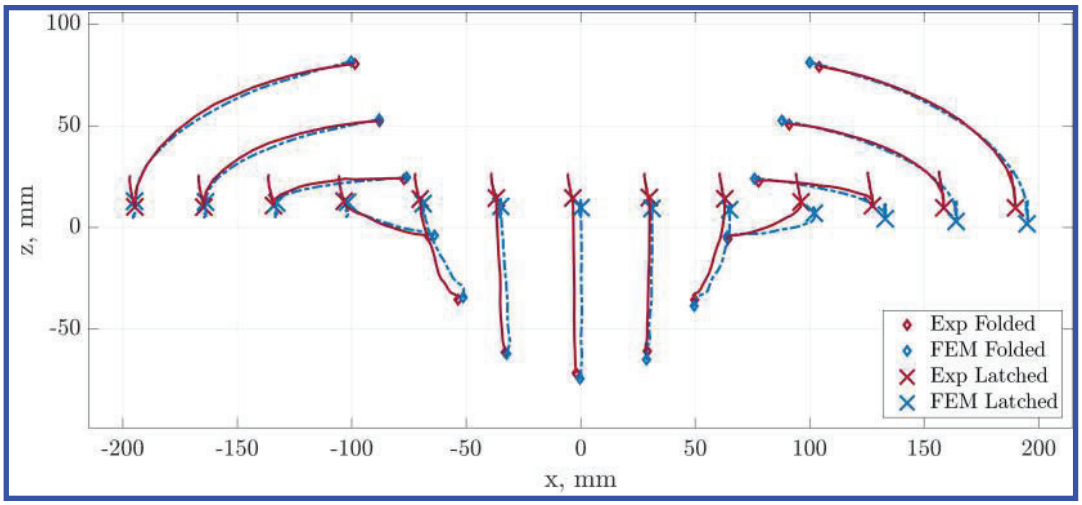

(a) Top view of the 13 lower longeron marker coordinates when unfolding from $\theta_0 = 134^o$.

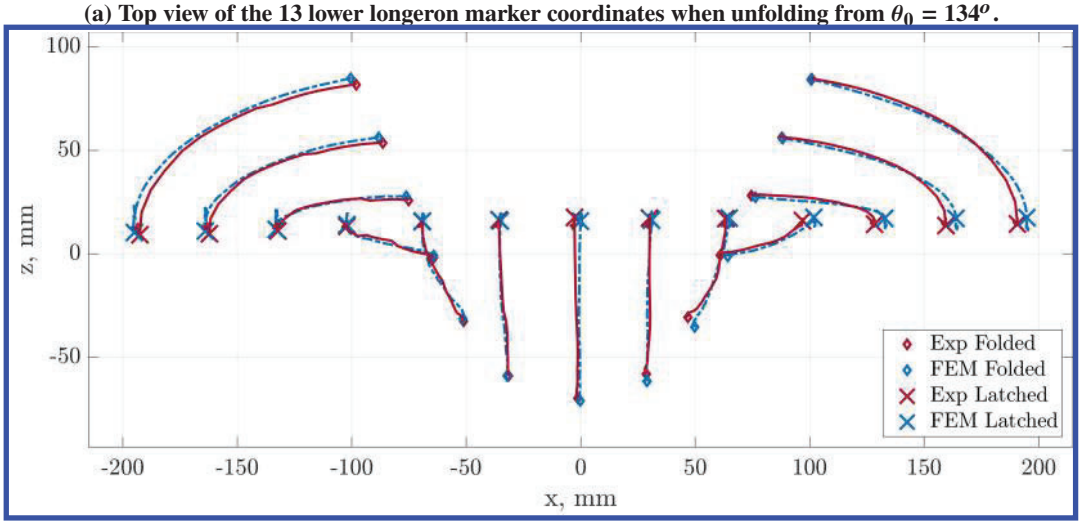

(b) Top view of the 13 upper longeron marker coordinates when unfolding from $\theta_0 = 134^o$.

Fig. 10 The initial folded shape from the FEM was validated by comparing longeron marker locations with experimental results, as well as the trajectories of the unfolding for upper and lower longerons respectively.

two longerons from 3 ms at $\theta_0 = 57^o$ to 11 ms at $\theta_0 = 45^o$. Note the exaggerated deceleration at small fold angles as compared with the low-fidelity FEM results in Fig. 11. This behavior becomes more pronounced as θ_0 approaches θ_c.

The qualitative behavior of the deployment also closely matched the experiments: the lower longeron decelerated faster than the upper one under spring tension, and the strip buckled torsionally by approximately 3^o after latching. If the initial angle was set to 41^o as opposed to 45^o, the FEM no longer latched, suggesting that small changes in the initial conditions may be enough to increase the critical angle to match the experiments.

3. FEM Refinement

One key assumption made by the FEM is that the springs act purely axially and have no plastic deformation. Retroreflective markers were placed at either end of each spring in order to track spring extension during the deployment. The resulting data suggests that the springs do not extend symmetrically (Fig. 13). There are several potential explanations for this. Firstly, alignment error when pre-tensioning the springs may have led to variations in initial extension. Second, the springs plastically deform with repeated extensions and therefore have a preferred buckling direction and out-of-plane behavior [5]. Lastly, the strip buckles torsionally due to the pre-tension after longeron latching, leading to asymmetries.

Unlike the experiments, the springs in the FEM extend symmetrically (Fig. 13). The FEM strip buckles torsionally

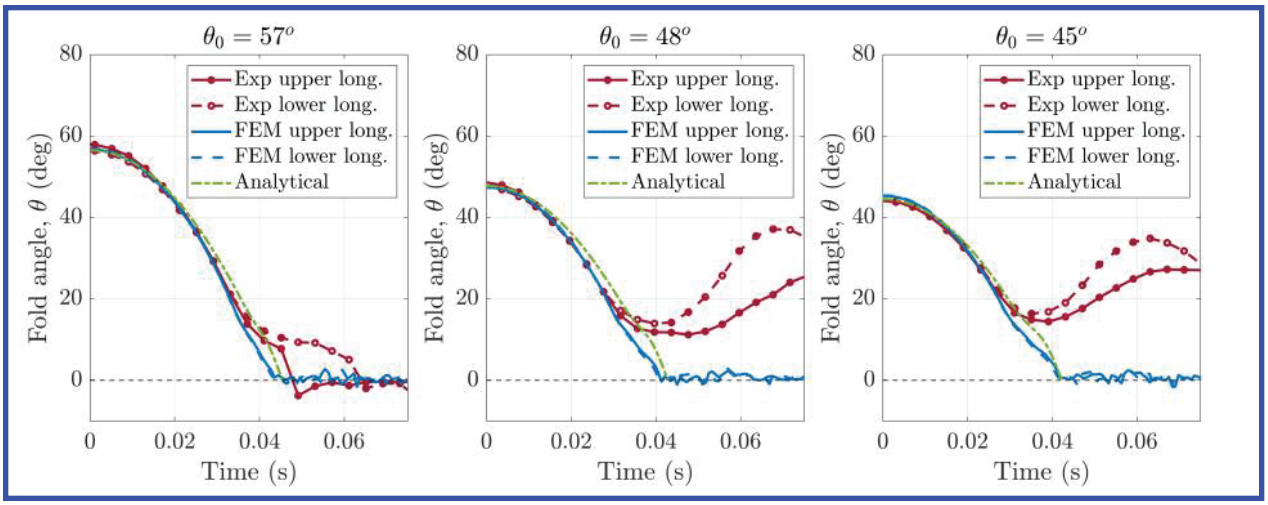

Fig. 11 For a strip unfolding with $F_0 = 2$ N and $e_0 = 2.5$ mm, the analytical model predicts latching for all three initial fold angles. A low-fidelity FEM validates the analytical results within 7^o, suggesting that higher fidelity is needed to capture unfolding dynamics.

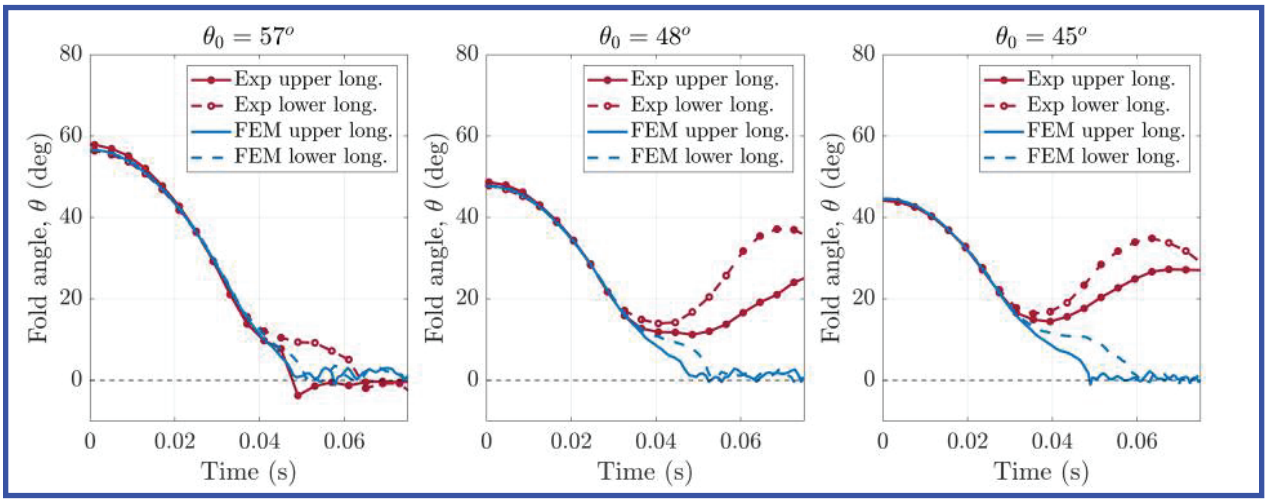

Fig. 12 For a strip unfolding with $F_0 = 2$ N and $e_0 = 2.5$ mm, the numerical model predicts latching for all three initial fold angles, therefore predicting a smaller θ_c than experimental results.

upon latching so the third explanation for the asymmetry is likely not significant. After repeated trials, introducing a 0.5 mm additional initial extension in one of the two springs greatly improved alignment with the experimental data (Fig. 14): The FEM correctly predicted latching vs. not latching for all three cases. For $\theta_0 = 48^o$ and $\theta_0 = 45^o$, the FEM predicted the minimum fold angle before the strip bounced back within 2^o for both longerons, however the deviation in between the two longeron fold angles after bouncing back is not as large as in the experimental results.

The 0.5 mm spring extension asymmetry is well within potential experimental alignment error during pre-tensioning, but may also serve to capture out-of-plane spring behavior.

4. Energy Analysis

For this simulation, keeping only the relevant terms, the energy balance is

$$E_S + E_A + E_{VD} + E_K - E_W = E_{tot} = 0 \tag{13}$$

where E_S is the strain energy, E_A is the artificial energy, E_{VD} is the energy from viscous damping, E_K is the kinetic energy, and E_W is the external work done on the system. The artificial energy is a term introduced to control hourglassing

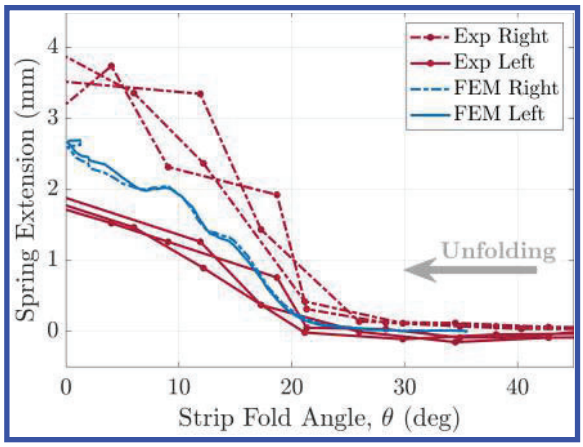

Fig. 13 Spring extension as a function of fold angle was measured experimentally. The springs come under tension at $\theta = 20^o$ and stretch asymmetrically until the longerons latch. This asymmetry does not occur in the FEM.

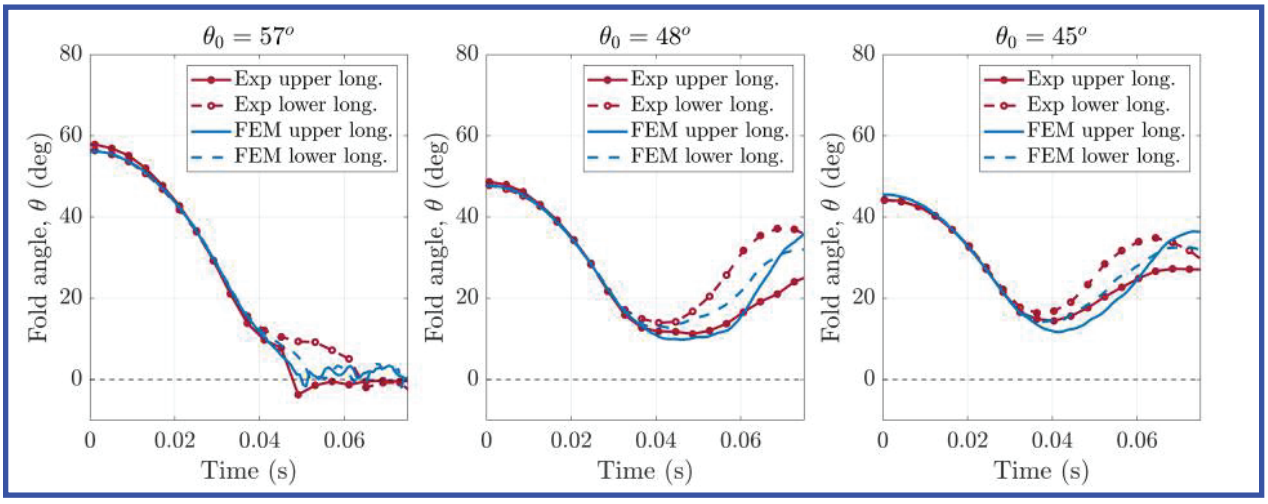

Fig. 14 Introducing an asymmetric initial spring extension of $e_0 = [2.5, 3]$ mm in the FEM allowed for accurate prediction of latching. For the non-latching cases, the FEM captured the minimum fold angle reached within 2^o for each longeron.

modes in the S4R shell elements and reduce mesh distortion. As a general rule for reliable simulation results, the artificial energy should be kept under 5% of the concurrent strain energy. As no additional energy is being added or removed during the simulation, we expect the total energy to remain constant for the duration of the entire simulation, and zero by Abaqus' convention.

For a simulation with $\theta_0 = 72^o$, $F_0 = 2$ N, and $e_0 = 2.5$ mm, the corresponding energy curves during the entire simulation are shown in Fig. 15. External work is done on the system to pinch the longerons (0-50 ms), causing an increase in strain energy. During the folding step (50-250 ms), there is a dip in the strain and external energies as the spring load decreases and the springs eventually lose tension. During the damping step (250-350 ms), the kinetic energy decreases to zero, as desired. During these first three steps, the artificial energy remains approximately zero.

For the same simulation, the deployment portion of the energy plot is expanded in Fig. 16a. For the duration of the deployment, the only varying terms (aside from the artificial energy) are the kinetic and strain energies so they mirror each other. While the springs are slack, the strip begins to unfold and the strain energy decreases until the springs come under tension. This local minimum in the strain energy is the first stable equilibrium point. The strain energy then increases as the applied spring moment is overcome (reaching the unstable equilibrium point at the local maximum) and then decreasing sharply as the longerons latch. At this point, higher frequency oscillations, accompanied by localized

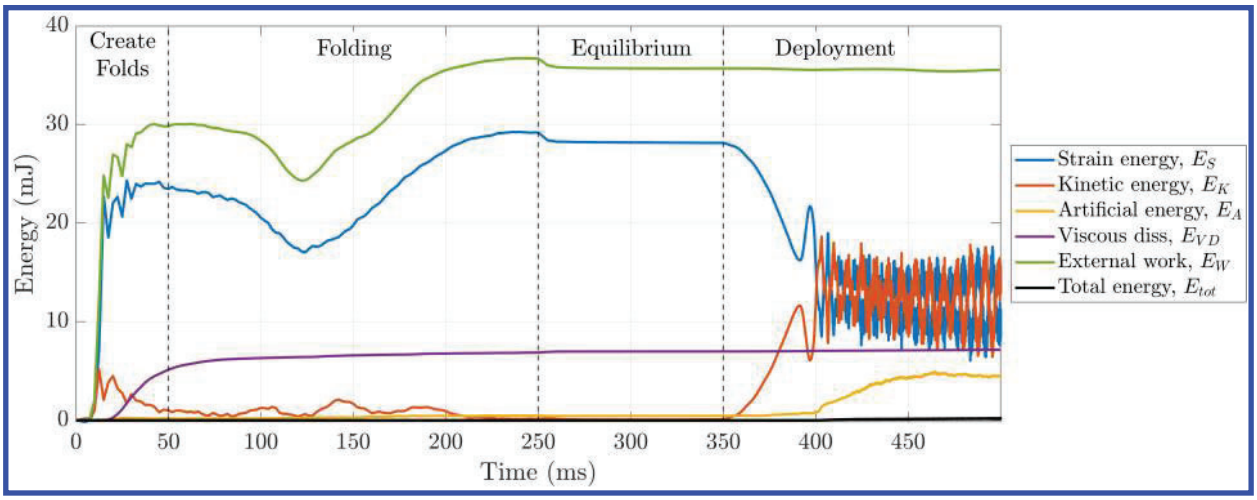

Fig. 15 Energy components for a simulated strip unfolding from $\theta_0 = 72^o$, $F_0 = 2$ N, and $e_0 = 2.5$ mm.

buckling and deformations in the strip longerons, dominate the rest of the simulation. Because of these oscillations and a lack of damping, the strain energy does not return to zero even though the strip has unfolded. These localized deformations also cause hourglassing which creates an increase in artificial energy above the 5% rule. This increase could not be mitigated by a reduced mesh size (1 mm instead of 2 mm) or a 10-fold smaller time step. We therefore consider this model to only stay accurate up until longeron latching.

By comparison, Fig. 16b shows the corresponding energy curves for the same strip and spring configuration unfolding from 41^o, a case where the longerons fail to latch. Note that the magnitude of strain energy at the beginning of deployment is smaller due to the smaller fold angle. The strain energy reaches a local minimum when the springs come under tension. This is again that stable equilibrium point, and we would expect the strain energy magnitude at this point to be the same regardless of the initial fold angle. Indeed, it is 16.2 mJ for the 41^o fold and 15.9 mJ for the 72^o strip. The difference between latching and not latching then comes from the larger kinetic energy at this point for a larger fold angle (11.6 mJ for 72^o compared to the much smaller 3.7 mJ for 41^o). Since the strip does not fall into high frequency oscillations in this case, the artificial energy remains small for the duration of the simulation.

5. Static Deployment Analysis

While we may be able to successfully model the deployment path of the dynamic unconstrained strip unfolding, the structure may encounter unexpected disturbances that cause it to deviate from this predicted path. In these cases, we wish to ensure that the structure cannot get stuck in an intermediate unfolding state. Thus, we must design the strip such that the only equilibrium state is the fully unfolded one. Returning to the moment analysis from Section III, the membrane tensioning mechanism must be designed such that the moments applied to the strip are strictly less than the internal strip moment for all fold angles.

Revisiting the plots of moment generated in the strip due to the spring, we explore the effect of different types of springs. Unlike the ideal force-extension plot originally shown in Fig. 3b, kirigami springs are not perfectly bilinear. In Fig. 17, we compare the force-extension behavior of the kirigami spring measured experimentally with a perfect constant-force spring and a linear spring, where all springs have a force of 1.34 N at an extension of 2 mm.

Constant-force springs create a triangular moment plot (Fig. 17b) where the maximum moment generated is when the spring first comes under tension. This is highly unfavorable as even for very small initial extensions, the maximum moment will occur before the longerons begin to latch (at which point the internal moment is small) and bear the risk of stopping deployment. By comparison, a linear spring has an approximately parabolic moment-angle relationship so it generates the largest moment when the strip is more likely to be latched. In addition, this maximum moment is only 39% of that of the constant-force spring even though both springs have the same load when the strip is fully unfolded.

Alternatively, we can explore the impact of various changes in strip geometry (such as increasing longeron or batten spacing, or modifying spring integration) on the applied spring moment. For this parametric study, we assume that the internal moment in the strip remains the same even though the overall geometry changes, since the longeron geometry itself is not changing.

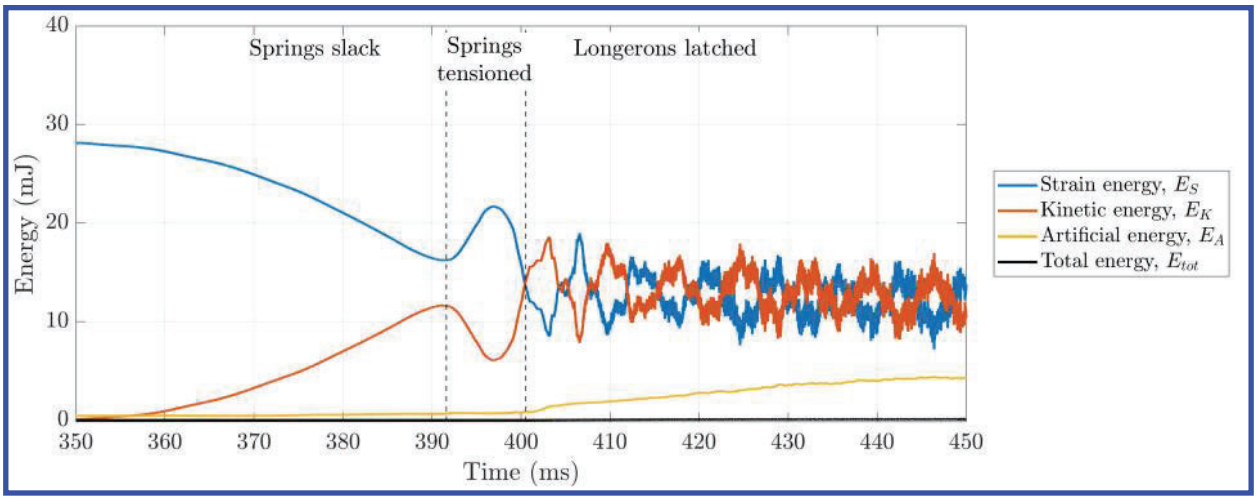

(a) Simulation energy balance unfolding from $\theta_0 = 72^o$

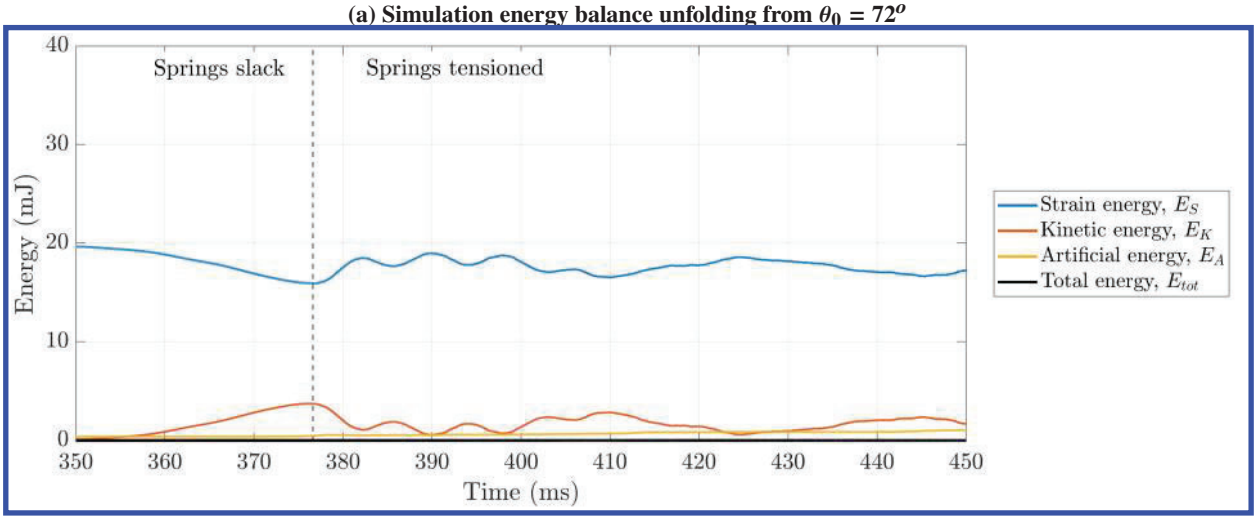

(b) Simulation energy balance unfolding from $\theta_0 = 41^o$

Fig. 16 The strip has an equilibrium point shortly after the springs come under tension where the strain energy reaches a local minimum of approximately 16.2 mJ. Larger initial fold angles mean the strip has greater kinetic energy at this equilibrium point, allowing the longerons to latch.

First off, the spring can be offset from the plane of the strip by a perpendicular distance t, towards the folding direction. As seen in Fig. 18, larger values of t cause a left-ward shift in the applied moment curve. This means the maximum moment now is reached at a smaller fold angle, which is preferable. Alternatively, if the offset is applied in the negative direction, the applied moment curve is shifted to the right. This offset causes a non-zero moment when the strip is fully unfolded, which may cause bending in the strip, leading to unfavorable membrane wrinkling.

An overall increase in the frame size causes the initial spring extension to be less prominent, meaning the effective inciting fold angle when the springs come under tension is smaller (Fig. 19). This however significantly increases the maximum moment generated. The strip aspect ratio could also be increased, elongating the square frame. This also decreases the effective inciting angle and increases the maximum moment (Fig. 20).

Finally, the longeron geometry itself could be modified to increase the internal moment. This could be achieved through different materials, composite layers, overall thickness, or increased flange angle.

To ensure predictable and successful deployment, it may be necessary to re-design the pre-tensioning mechanism such that deployment occurs even under quasi-static conditions. While kirigami springs are not perfectly constant-force, they still have a steeper increase in moment when first coming under tension, and reach a greater maximum moment than a comparable linear spring. Unless small loads and extensions can be used, kirigami springs may not be the optimal choice for tensioning the membrane.

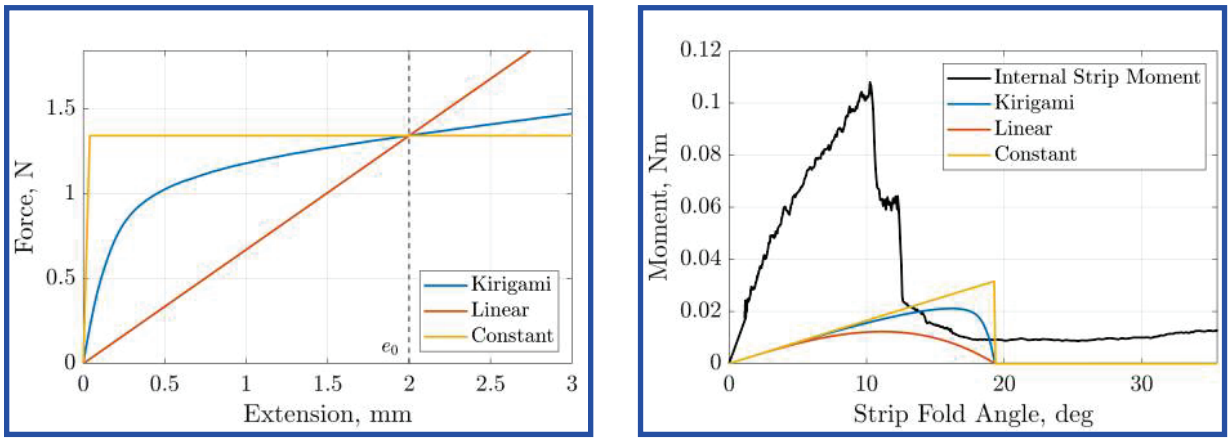

(a) Spring force-extension profile

(b) Moment magnitude about strip hinge

Fig. 17 Constant-force springs cause a sudden increase in moment at first extension. For the same unfolded load and extension, linear springs generate only 39% of the maximum moment.

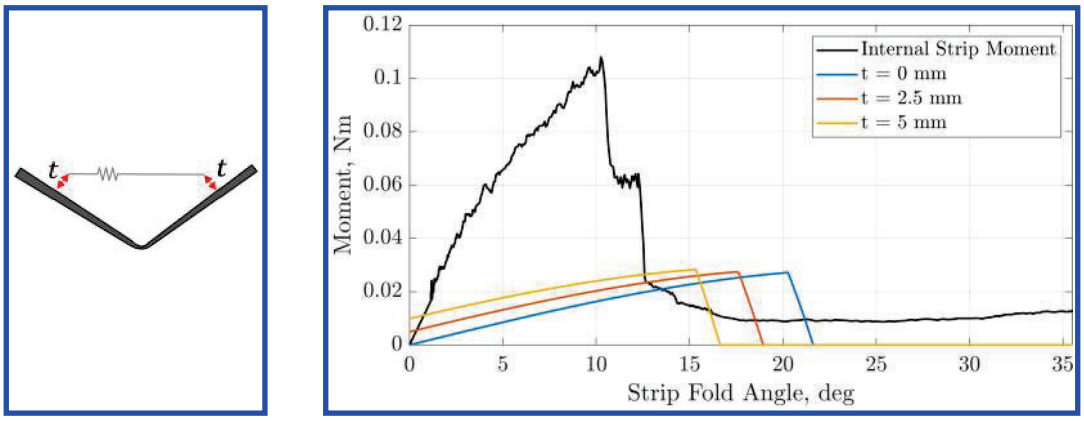

Fig. 18 Adding a perpendicular offset to the springs shifts the applied moment curve to the left, decreasing the angle at which the springs come under tension. The moment is no longer zero when the strip is fully unfolded.

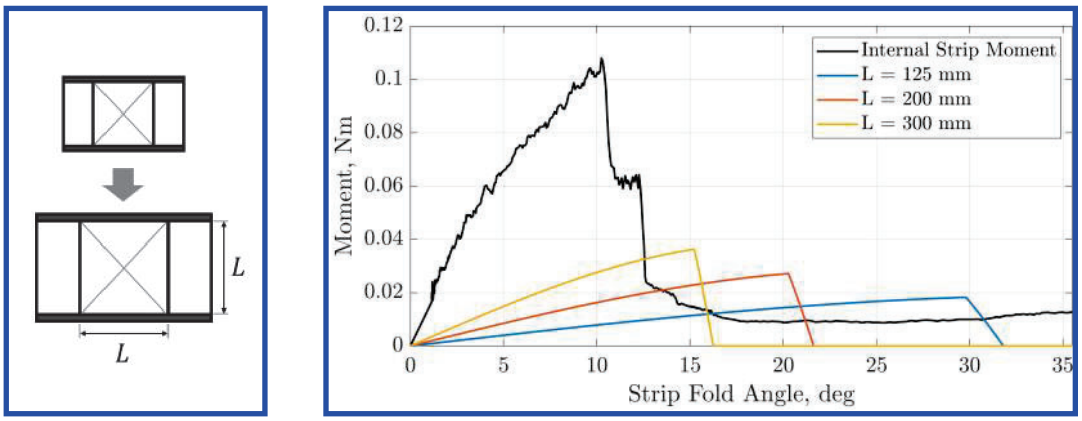

Fig. 19 Increasing the overall strip size decreases the angle at which the springs come under tension but increases the maximum applied moment.

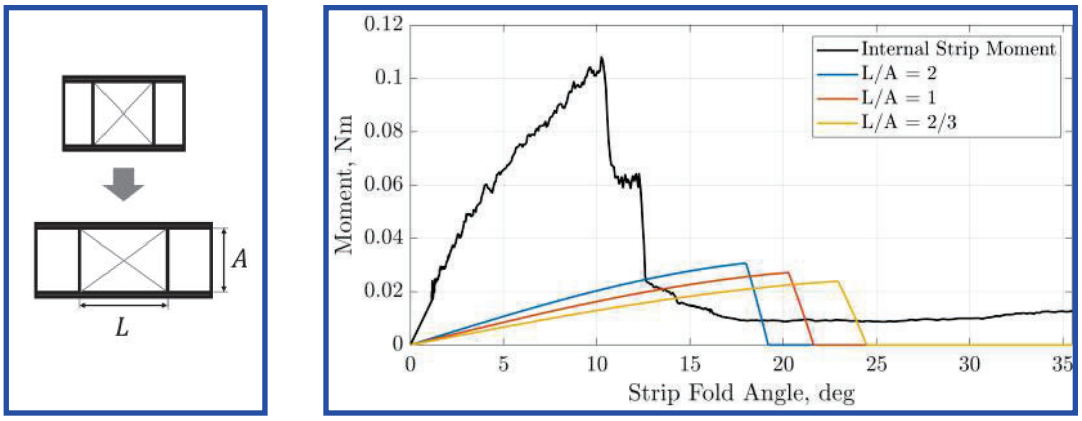

Fig. 20 Increasing the L/A ratio decreases the angle at which the springs come under tension but increases the maximum applied moment.

VI. Conclusion

Ladder-like composite strips are the basis for the lightweight deployable space solar arrays that make up the Caltech Space Solar Power Project. These strips support a functional membrane that is pre-tensioned to avoid buckling under adverse thermal loads on orbit. Since the structure deployment is self-powered using stored elastic strain energy from folding, the requirement to pre-tension the membrane using springs can potentially impede the unconstrained deployment of the structure.

In this work, we designed an experimental procedure to test the impact of unfolding in the presence of diagonal pre-tensioned springs on a composite ladder-like strip. For the experiments, we chose a spring pre-tension of 2 N at an extension of 2.5 mm that creates two intermediate equilibrium states that may prevent longeron latching. Thus dynamics are critical to complete unfolding and latching: if the initial fold angle is large enough, the strip will have enough kinetic energy to overcome the strain energy barrier from spring tension and reach full deployment. We developed an analytical model based on kinematic analysis, as well as a numerical model using the dynamic exlicit solver in Abaqus, to predict and understand the deployment behavior. Due to the simplicity of our experimental setup, model accuracy was highly dependent on accurately replicating the initial state of the experiment. By introducing an asymmetry in spring pre-extension, we were able to capture the asymmetries observed in the experiments and achieve better performance of the FEM simulations, predicting the critical angle to within a few degrees.

In order to minimize risks to deployment, the springs should not create static equilibrium states in the structure at intermediate stages of unfolding. To achieve this, the internal strip moment must always be greater than the applied moment induced by the springs. We have shown that near constant-force springs, such as the kirigami springs used in the current tensioning architecture, induce large moments before the strip latches and may prevent full deployment under small initial fold angles. Extension springs that are quasi-linear generate smaller overall moments and act at smaller fold angles for the same pre-load and initial extension. The continued use of kirigami springs as the pre-tensioning mechanism would require changes in strip geometry to ensure proper deployment under all conditions.

Acknowledgments

The authors would like to thank Alan Truong for fabricating the test structure and George Popov for his help characterizing kirigami springs. This research was funded by the Space Solar Power Project at Caltech.

References

[1] Pedivellano, A., and Pellegrino, S., "Deployment Dynamics of Thin-Shell Space Structures," *Journal of Spacecraft and Rockets*, Vol. 59, No. 4, 2022, pp. 1214–1227. https://doi.org/10.2514/1.A35172.

[2] Pedivellano, A., Gdoutos, E., and Pellegrino, S., "Sequentially Controlled Dynamic Deployment of Ultra-Thin Shell Structures," *AIAA Scitech 2020 Forum*, American Institute of Aeronautics and Astronautics, Orlando, FL, 2020. https://doi.org/10.2514/6.2020-0690.

[3] Royer, F., and Pellegrino, S., "Ultralight Ladder-type Coilable Space Structures," *2018 AIAA Spacecraft Structures Conference*,

American Institute of Aeronautics and Astronautics, Kissimmee, Florida, 2018. https://doi.org/https://doi.org/10.2514/6.2018-1200.

[4] Murphey, T. W., and Banik, J., "Triangular rollable and collapsible boom," , Mar. 2011. US Patent 7,895,795.

[5] Faschinger, T., "Integration of Thin-Film Photovoltaics into Ultralight Deployable Space Structures," Master's thesis, ETH Zurich, May 2022.

[6] Isobe, M., and Okumura, K., "Initial rigid response and softening transition of highly stretchable kirigami sheet materials," *Scientific Reports*, Vol. 6, No. 1, 2016, p. 24758. https://doi.org/10.1038/srep24758.

[7] Leclerc, C., and Pellegrino, S., "Nonlinear elastic buckling of ultra-thin coilable booms," *International Journal of Solids and Structures*, Vol. 203, 2020, pp. 46–56. https://doi.org/10.1016/j.ijsolstr.2020.06.042.

[8] Reddy, N. H., and Pellegrino, S., "Dynamics of the Caltech SSPP deployable structures: structure-mechanism interaction and deployment envelope," *AIAA Scitech 2023 Forum*, American Institute of Aeronautics and Astronautics, 2023. https://doi.org/10.2514/6.2023-2065.

[9] "Motion Capture Systems," , 2023. URL http://optitrack.com/index.html.